Studying Altocumulus with Ice Virga Using Ground-Based Active and Passive Remote Sensors

Zhien Wang

Goddard Earth Science and Technology Center, University of Maryland, Baltimore County, Baltimore, and Mesoscale Atmospheric Processes Branch, NASA Goddard Space Flight Center, Greenbelt, Maryland

Kenneth Sassen

Geophysical Institute, University of Alaska Fairbanks, Fairbanks, Alaska

David N. Whiteman and Belay B. Demoz

Mesoscale Atmospheric Processes Branch, NASA Goddard Space Flight Center, Greenbelt, Maryland

ABSTRACT

Mixed-phase clouds are still poorly understood, though studies have indicated that their parameterization in general circulation models is critical for climate studies. Most of the knowledge of mixed-phase clouds has been gained from in situ measurements, but reliable remote sensing algorithms to study mixed-phase clouds extensively are lacking. A combined active and passive remote sensing approach for studying supercooled altocumulus with ice virga, using multiple remote sensor observations, is presented. Precipitating altocumulus clouds are a common type of mixed-phase clouds, and their easily identifiable structure provides a simple scenario to study mixed-phase clouds. First, ice virga is treated as an independent ice cloud, and an existing lidar–radar algorithm to retrieve ice water content and general effective size profiles is applied. Then, a new iterative approach is used to retrieve supercooled water cloud properties by minimizing the difference between atmospheric emitted radiance interferometer (AERI)–observed radiances and radiances, calculated using the discrete-ordinate radiative transfer model at 12 selected wavelengths. Case studies demonstrate the capabilities of this approach in retrieving radiatively important microphysical properties to characterize this type of mixed-phase cloud. The good agreement between visible optical depths derived from lidar measurement and those estimated from retrieved liquid water path and effective radius provides a closure test for the accuracy of mainly AERI-based supercooled water cloud retrieval.

1. Introduction

Clouds not only play crucial roles in regulating the earth–atmosphere system energy budget, but also the atmospheric hydrological cycle. The impact of a cloud system strongly depends on the cloud microphysical properties and its vertical extent (Stephens et al. 1990; Baker 1997). Although clouds can contain only water droplets when $>0°C$ and only ice crystals when $<-40°C$, between $0°$ and $-40°C$ clouds can be of ice, water, or mixed-phase composition (Rauber and Tokay 1991; Cober et al. 2001). Cloud properties associated with different cloud phases within this temperature range are complicated and are not well known. However, properly representing them in general circulation mod-

els (GCMs) is very important for climate simulation. Fowler et al. (1996) show that the variation of glaciation temperature from $0°$ to $-40°C$ in a GCM simulation yielded about 4 and -8 W m^{-2} differences in the top-of-atmosphere longwave and shortwave cloud radiative forcing, respectively. Other studies (Li and Le Treut 1992; Sun and Shine 1994; Gregory and Morris 1996) have also shown that the treatment of mixed-phase clouds in GCMs affects either their climate sensitivity or their mean climate impact.

Mixed-phase clouds have been studied mainly with in situ measurements (Hobbs and Rangno 1985; Heymsfield et al. 1991; Sassen 1991; Pinto 1998; Field 1999; Cober et al. 2001; Lawson et al. 2001; Fleishauer et al. 2002), which provide detailed microphysical properties to understand the physical processes controlling mixed-phase clouds. However, it is very expensive to accumulate large in situ datasets over long time periods and in different climate regions. Existing remote sensing algorithms of mixed-phase clouds (Sauvageot 1996; Vi-

Corresponding author address: Zhien Wang, UMBC/GEST Center, Code 912, NASA GSFC, Building 33, Room A417, Greenbelt, MD 20771.
E-mail: zhien@agnes.gsfc.nasa.gov

vekanandan et al. 1999) are not practical for many stratiform mixed-phase clouds. Therefore, it is necessary to develop reliable new ground-based and space-based remote sensing algorithms for mixed-phase cloud study. Recent developments and integrations of remote sensor technologies provide the possible means to achieve this challenging task. The Department of Energy Atmospheric Radiation Measurement Program (ARM) Cloud and Radiation Test Bed (CART) sites have been established in three climatic regimes: the southern Great Plains (SGP), the tropical western Pacific (TWP), and the North Slope of Alaska (NSA) (Stokes and Schwartz 1994). The continuous high-quality data streams from different passive and active remote sensors at these CART sites provide the opportunity to study mixed-phase clouds in these dissimilar climate regimes. Turner et al. (2003) recently presented an approach to study Arctic mixed-phase clouds with atmospheric emitted radiance interferometer (AERI) measurements.

In this study, we begin our algorithm-developing effort from studying a simple type of mixed-phase cloud: supercooled altocumulus with ice virga. According to the cases studied by Fleishauer et al. (2002) and the University of Utah facility for atmospheric remote sensing (Sassen et al. 2001) and CART data streams, this is a common type of midlevel mixed-phase cloud in all regions and also provides a simple scenario to understand better all varieties of mixed-phase clouds (Gedzelman 1988). A combined active and passive remote sensing approach is presented here to study altocumulus plus ice virga, using data from the SGP and NSA CART sites. In this approach, we apply an existing lidar–radar algorithm to retrieve ice virga properties (Wang and Sassen 2002a) and develop a new approach to retrieve supercooled water cloud properties. This paper is organized in the following way. First, instruments used in this study are briefly discussed in section 2. The detailed approach of combined active and passive remote sensing is presented in section 3. Then, the capabilities of this approach are demonstrated in section 4 through two case studies at the NSA and SGP CART sites. Our conclusions are given in section 5.

2. Instruments

a. Millimeter-wavelength cloud radar

The millimeter-wavelength cloud radar (MMCR) is a zenith-pointing radar with a 2-m-diameter antenna that operates at 34.86 GHz (8.7-mm wavelength); it has a sensitivity of about −50 dBZ at 5.0-km altitude (Moran et al. 1998). This powerful Doppler radar, working in cycles of four sequential modes with selectable parameters, can detect most of the clouds in the troposphere from stratus to cirrus. Cloud detection at 8 mm has some distinct advantages when compared with lidar and shorter-wavelength radars. For example, MMCR can penetrate optically thick clouds to detect multilayer cloud systems. However, its long wavelength limits its capability to detect midlevel supercooled water clouds with relatively small water droplets. For mixed-phase clouds or water clouds with drizzle, MMCR signals are dominated by the backscatter of ice particles or drizzle-size droplets.

b. Raman lidar

The SGP CART site Raman lidar measures water vapor, aerosol, and cloud profiles simultaneously (Whiteman et al. 1992; Goldsmith et al. 1998) and is a powerful tool for atmospheric remote sensing. This system uses a tripled neodimium-doped yttrium–aluminum–garnet (Nd:YAG) laser transmitter (354.7 nm) and detects Raman-backscattered light from water vapor (3657 cm^{-1}) and nitrogen (2329 cm^{-1}) molecules, plus elastic backscattered light from molecules and particles. Its dual-field-of-view design provides a large detectable signal range to cover the whole troposphere with excellent daytime capability without sacrificing nighttime performance. This Raman lidar system is fully computer automated and runs unattended following a simple, brief (~5 min) start-up period.

c. Micropulse lidar

The micropulse lidar (MPL) is a compact eye-safe lidar that measures cloud-base heights and aerosol profiles from the surface to about 20 km in the absence of strongly attenuating clouds (Spinhirne 1993). Eye safety allows for full-time, long-term unattended operation and is achieved by transmitting low power pulses through an expanded beam, with a much higher pulse repetition frequency than that used in standard lidar systems. The low pulse energy limits its ability for high cloud measurements during daytime with high background signals, however. On the other hand, its unattended operation and negligible multiple scattering effects make it a valuable system for cloud studies, especially at the TWP and NSA sites, where MPL is the only currently available lidar system. Cloud-layer transmittance can be calculated from lidar measurements when clear air returns above cloud top are available, permitting cloud-layer optical depth to be estimated.

d. Microwave radiometer

The microwave radiometer (MWR) receives nadir microwave radiation from the sky at 23.8 and 31.4 GHz. Measurements are recorded as atmospheric brightness temperatures with a radiometric range of 0–700 K and an accuracy of 0.3 K. Cloud liquid water in the atmosphere emits in a continuum that increases with frequency, dominating the 31.4-GHz observation, whereas water vapor dominates the 23.8-GHz channel. The water vapor and liquid water signals can, therefore, be separated by observations at these two frequencies (Hogg

et al. 1983). Statistical retrieval methods are usually employed to derive water vapor path and liquid water path (LWP) from the total absorption. In current ARM data, the regression residual error or ''theoretical accuracy'' of LWP is about 0.03 mm (30 g m^{-2}), or 10 times the sensitivity or noise limit (0.003 mm) of MWR. This detectable level limits MWR capability to measure LWP in many midlevel supercooled clouds and mixed-phase clouds.

e. AERI

The ''heart'' of the AERI radiometer is a Fourier transform infrared (IR) spectrometer, including the calibration blackbodies with temperature controllers. The AERI measures the absolute infrared spectral radiance of the sky also in the nadir direction. The spectral measurement range of the instrument is 500–3300 cm^{-1} (20–3 μm), with a spectral resolution of 1.0 cm^{-1}. The instrument field of view is 1.3°. A calibrated sky radiance spectrum is produced every 10 min. AERI has been used for a variety of cloud studies (Mace et al. 1998; Smith et al. 1993; Turner et al. 2003).

3. Algorithm description

Altocumulus cloud with ice virga can be generally regarded as two connected cloud layers, where the top is the water-dominated source cloud and the bottom is an ice cloud, although it is also necessary to study ice within the water-dominated source cloud. In this section, we discuss details of the algorithms to retrieve the microphysical properties of ice virga and water-dominated source cloud through combined ground-based active and passive remote sensing.

a. Ice virga

We treat ice virga below the water-dominated source cloud as cirruslike ice clouds and apply a previous lidar–radar algorithm (Wang and Sassen 2002a) to derive the ice water content (IWC) and general effective size (D_{ge}) profiles. In the lidar–radar algorithm, IWC and D_{ge} are retrieved from the radar reflectivity factor Z_e and cloud extinction coefficient σ estimated from lidar measurements. MMCR typically detects the relatively strong signals from ice virga because of their large particle sizes, despite their low concentrations. However, ice virga are usually optically thin, and so it is a challenge to estimate the σ of ice virga accurately, even from Raman lidar measurements. We normally need to estimate σ of the virga from the backscattering coefficient by assuming an extinction-to-backscattering ratio (lidar ratio). Uncertainties in the lidar ratio unavoidably result in some uncertainties in σ, leading to uncertainties in retrieved IWC and D_{ge}. Statistics of measured lidar ratios from the combined lidar and infrared radiometer method and Raman lidar indicate that values in cirrus clouds

are most likely within the range of 15–20 and slightly depend on cloud temperature (Sassen and Comstock 2001). Therefore, the accuracy of σ estimated from the backscattering coefficient, using a lidar ratio of 18, should be reasonable statistically. Another possible error source in σ is multiple-scattering effects on the backscattering coefficient measurements. This error source is not a significant problem for ground-based remote sensing because the laser pulse penetrates the optically thin ice virga before entering the optically thick water-dominated source cloud, where multiple scattering starts to play an important role for lidar systems with a relatively large field of view (e.g., >0.5 mrad).

b. Supercooled water-dominated source cloud

The radiative properties of water cloud layers can be derived from two basic parameters: LWP and cloud droplet effective radius r_{eff}. However, altocumulus clouds usually have small LWP values, which are often too small for current MWR to detect (Wang and Sassen 2001). Thus, it is best to rely on other instruments, such as AERI and lidar. Unlike stratus or stratocumulus clouds, which are often too optically thick for lidar to penetrate, supercooled altocumulus clouds can often be penetrated by lidar to measure cloud-layer physical and optical depths and cloud optical properties (Young et al. 2000). Although they have small LWP, altocumulus clouds emit significant signals in the IR window region, which AERI can generally detect. The general principles and basic retrieval steps to use AERI for cloud studies are discussed by Smith et al. (1993), and a combination of AERI with lidar or MMCR measurements has been used for cirrus studies (Mace et al. 1998; DeSlover et al. 1999). Here, we discuss an optimal approach for combining AERI, lidar, and radar measurements to derive LWP and r_{eff} for altocumulus clouds with ice virga.

The changing water and ice refractive indices within the IR window region (8–13 μm) provide rich information for cloud studies, such that IR radiances within this region are widely used for cloud property retrieval (Strabala et al. 1994; Ackerman et al. 1995). Figure 1 shows the real and imaginary refractive indices of water across the atmospheric IR window. The absorption capability of a particle mainly depends on its imaginary refractive index. This figure reveals that the imaginary refractive index of water decreases from approximately 0.35 to approximately 0.035 as the wavenumber increases. The coexistence of these relatively small and large imaginary indices results in a large difference in water droplet absorption capability and cloud-layer IR emittance at different wavelengths. This fundamental principle allows us to retrieve the properties of optically thin water clouds.

In situ measurements have indicated that water droplets have r_{eff} from about 4 up to 15 μm (Heymsfield et al. 1991; Lawson et al. 2001; Fleishauer et al. 2002). Therefore, observations within the IR window contain
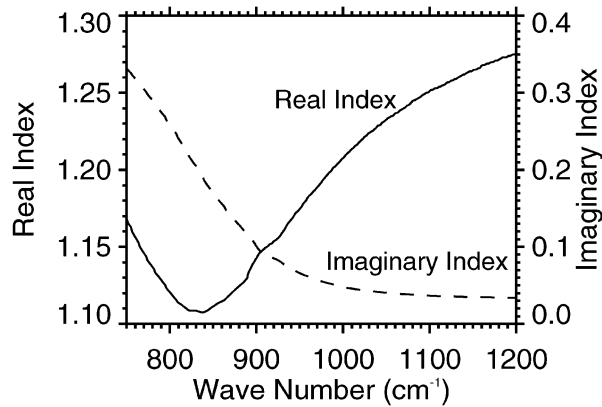
Fig. 1. The real and imaginary refractive indices of water across the atmospheric IR window.

sensitive information for the study of droplet size according to Mie theory. Figure 2 presents cloud droplet extinction and absorption efficiencies as a function of sphere radius for the wavelengths listed in Table 1. Extinction efficiencies at weakly absorbing wavelengths increase with size until reaching their maximums and then decrease to a constant value of approximately 2.0. In contrast, extinction efficiencies of strongly absorbing wavelengths increase with size and then approach a constant value. For absorption efficiency, strong absorption causes a peaked structure at several radii. It is clear that different wavelengths reach their peak extinction and absorption efficiencies at different droplet sizes, making IR window observations of water clouds promising. It is possible to retrieve more detailed size information rather than r_{eff}, but as the first step in our mixed-phase cloud study we only attempt to retrieve r_{eff}.

To minimize the possible random errors and to take advantage of information contained within different wavelengths and the high spectral resolution of AERI, we select 12 low atmospheric absorption wavelengths between atmospheric absorption lines ranging from 772 to 1160 cm^{-1} (Table 1). Then, we search for solutions of LWP and r_{eff} through minimizing the function F, defined as

$$F = \sum_{i=1}^{12} \left[\frac{I'(\lambda_i)}{I(\lambda_i)} - 1 \right]^2, \qquad (1)$$

where $I(\lambda_i)$ and $I'(\lambda_i)$ are the measured and calculated downward radiances at wavelength λ_i, respectively. Here $I'(\lambda_i)$ is calculated using the discrete-ordinate radiative transfer model (DISORT) package (Stamnes et al. 1988), with inputs that include water cloud optical properties parameterized as a function of LWP and r_{eff}, cloud temperature determined from radiosonde temperature profile and lidar–radar-identified cloud height, ice virga properties estimated from retrieved IWC and D_{ge}, and the molecular absorption optical depth profile obtained from the Moderate-Resolution Transmittance Model and Code (MODTRAN; Berk et al. 1998).
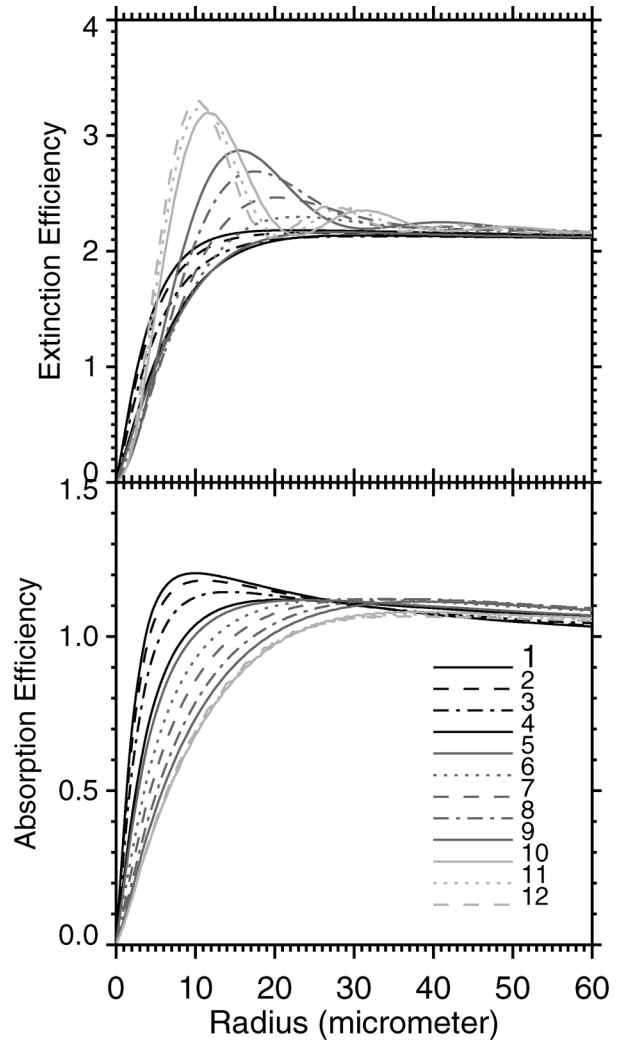

Fig. 2. Water droplet extinction and absorption efficiencies as a function of water droplet radius for wavelengths listed in Table 1.

Table 1. Selected AERI wavelengths for altocumulus cloud retrieval.

	Wavenumber (cm^{-1})	Wavelength (μm)
1	772	12.95
2	790	12.66
3	820	12.20
4	862	11.60
5	875	11.43
6	900	11.11
7	930	10.75
8	960	10.42
9	990	10.10
10	1090	9.17
11	1130	8.85
12	1160	8.62

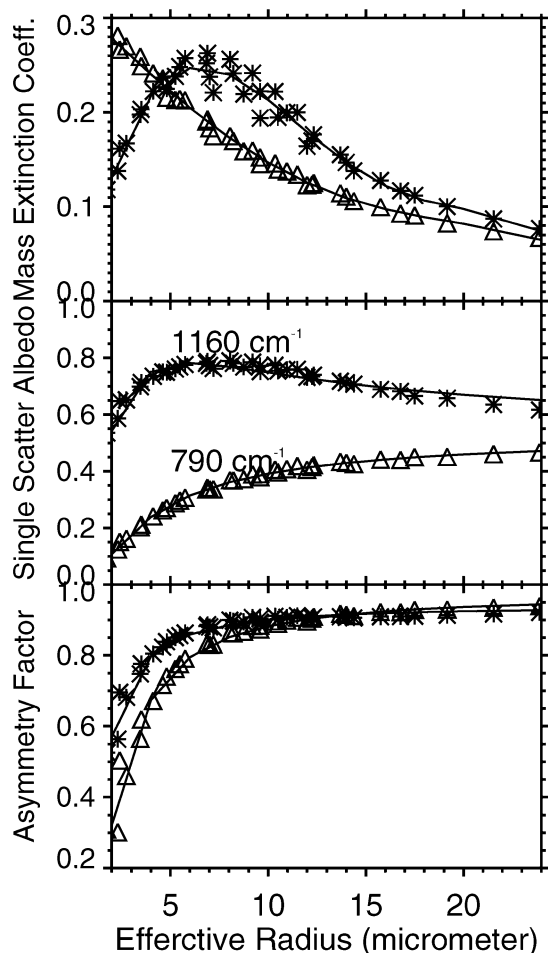FIG. 3. The k, ω, and g as function of r_{eff} for a weak (1160 cm^{-1}) and a strong (790 cm^{-1}) absorption wavelength by assuming lognormal size distribution, where solid lines are fitted results.

FIG. 4. A 2D display of F as a function of LWP and r_{eff}.

multaneously. To speed up the minimization procedure and maintain the accuracy of the solution, we search for an initial guess using two wavelengths and then search for the final solution within a narrow range of the initial guess with 12 wavelengths using fine steps of LWP and r_{eff}.

One limitation of using AERI downward radiance to study clouds is that cloud emissivity should be less than unity. Figure 5 presents emissivity as a function of LWP for two different r_{eff} values, which clearly shows that the slope of the emissivity to LWP decreases as LWP increases. The larger the slope of the emissivity to LWP is, the better is the accuracy of retrieved LWP. To maintain good retrieval accuracy, it is better that the cloud has an emissivity of less than 0.8, at least for the less-absorbing wavelengths. This means that absorption optical depth at the strongly absorbing IR wavelengths should be less than ~3. Differences between Figs. 5a and 5b suggest that the upper limit of retrievable LWP is strongly dependent on r_{eff}, and we can at least retrieve LWP up to 30 g m^{-2} for r_{eff} = 5.25 μm. Therefore, AERI measurements can cover the lower end of LWP values that the MWR is unable to measure, and we will show this point again in the case studies that follow.

The main error sources in the water-dominated source cloud retrieval are measurement errors in radiances and cloud temperature, errors in the estimated ice virga properties, and the errors associated with a change of water vapor with time. The effect of temporal variations of water vapor can be partially corrected for with the total precipitable water measured by the MWR (Comstock and Sassen 2001) or temporal profiles measured by Raman lidar. The measurement errors in radiances can be divided into random error and systematic measurement errors—the latter caused by instrument calibration and other factors. Simulations based on the case studies discussed below indicate that a ±1% systematic calibration error in all wavelengths causes about 3.1% and 2.4% mean errors in LWP and r_{eff}, respectively. Random measurement errors are simulated with zero means and the standard deviations of 2% of measured radiances, which can result in 2.4% and 5.0% errors in LWP and r_{eff}, respectively. The impact of errors in the estimated ice

The required cloud properties of each layer in the DISORT package are cloud optical depth, single-scatter albedo ω, and asymmetry factor g for phase functions calculated using the Henyey–Greenstein approximation. In the retrieval, the optical depth of the water-dominated layer is calculated with the LWP and cloud mass extinction coefficient k. Figure 3 plots k, ω, and g as a function of r_{eff} for a weak (1060 cm^{-1}) and strong (790 cm^{-1}) absorption wavelength by assuming a lognormal drop size distribution. The solid lines in Fig. 3 are fitted curves. For all 12 wavelengths, k, ω, and g are fitted as functions of r_{eff}, and so required water cloud inputs for DISORT are supplied with knowledge of LWP and r_{eff}. For the ice virga radiative properties, we use the parameterization developed by Fu et al. (1998) based on IWC and D_{ge}, which come from the lidar–radar algorithm.

Figure 4 presents an example of F as a function of LWP and r_{eff}. The existence of single minima in the 2D display of F indicates that it is both feasible and necessary to search for the solutions of LWP and r_{eff} si-
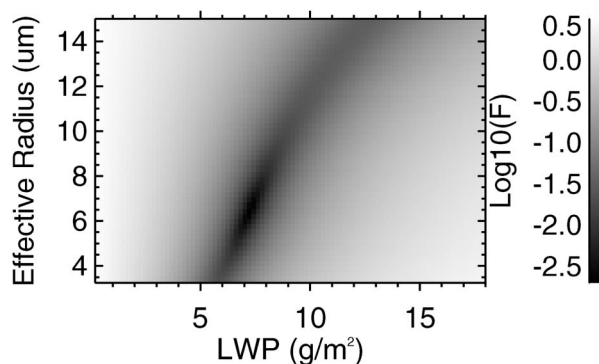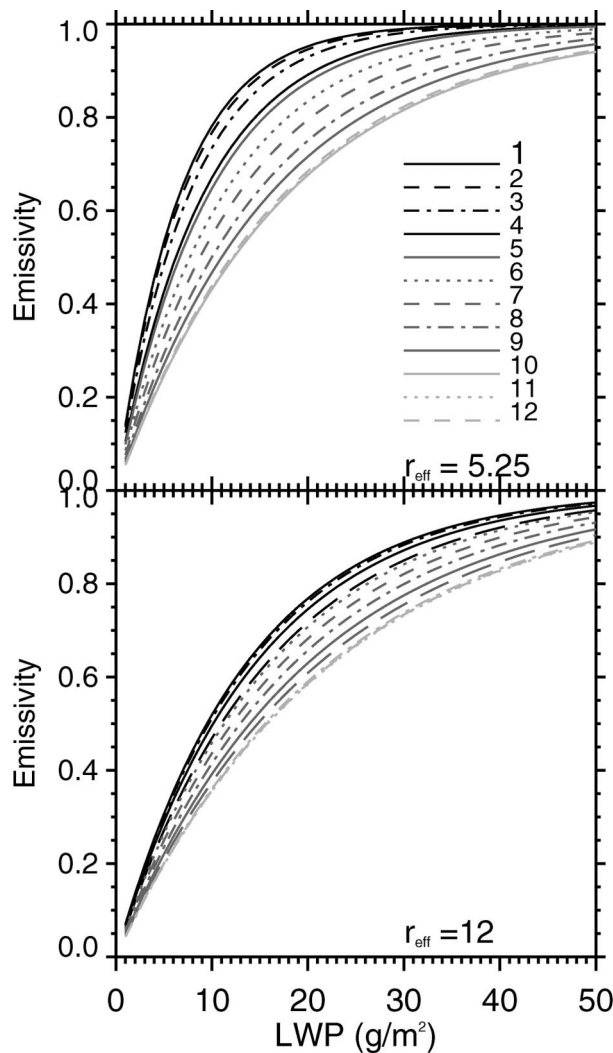
FIG. 5. The emissivity of water clouds as a function of LWP for two different r_{eff} values and wavelengths listed in Table 1.

virga properties on LWP and r_{eff} retrieval depends on ice contribution to the overall cloud optical depth and increases with the increasing of ice contribution. For the first case studied below, a 20% error in ice optical depth causes approximately 5% errors in them. In a similar way, a $\pm 1°C$ cloud temperature error also results in 2.8% and 3.3% errors. Ice crystals within the water-dominated thin cloud layer are not expected to have noticeable impacts on the LWP and r_{eff} retrieval; however, they are important to understand ice generation processes. Based on these simulations, we estimate uncertainties in retrieved LWP and r_{eff} of less than approximately 18%.

There is a simple relationship between LWP and visible optical depth τ:

$$\tau = \frac{3}{2\rho} \frac{LWP}{r_{eff}}, \qquad (2)$$

where ρ is water density. If the cloud is optically thin ($\tau <$ about 3), τ can be derived from lidar measurements. With negligible multiple scattering effects, as is often the case with MPL because of its narrow field of view, the lidar-derived τ can have good accuracy. Although combining τ with LWP derived from MWR measurements can also be used to derive r_{eff} from Eq. (2), current MWR designs cannot provide reliable low LWP values. Therefore, we only use lidar-derived τ as a closure test to examine the retrieval accuracy of LWP and r_{eff} here.

4. Case studies

a. 18 January 2000 at the NSA CART site

The first case we examine is from the NSA CART site. At this site, it appears that altocumulus with ice virga happens more commonly than at the midlatitude CART site and can last for more than 10 h, as in the case we study here. During 18 January 2000, a precipitating altocumulus appeared at ~0500 UTC and gradually dissipated at the end of day when high clouds moved in. Figures 6a–c show Z_e, mean Doppler velocity, and the logarithm of MPL returned power between 0400 and 1200 UTC. The differences between the lidar and radar signals result from the different number concentrations and particle sizes in the water and ice clouds and their different backscattering efficiencies with respect to the different remote sensor wavelengths. The supercooled water–dominated source cloud is indicated by the strong MPL signal and relatively weak Z_e stemming from a high concentration of small droplets. The black lines in Fig. 6 represent the supercooled water–dominated cloud base determined from MPL measurements (Wang and Sassen 2001). It is clear that the ice virga below the source cloud is strong and stable. Relative humidity, temperature, and potential temperature profiles from a radiosonde launched at 1831 UTC are presented in Fig. 7. During this time, the cloud base descended to about 2 km from its initial ~3-km base height. The temperature profile shows a temperature inversion of more than 3°C at the cloud top, and the potential temperature profile indicates a moist stable layer below the inversion.

The retrieved IWC and D_{ge} profiles are displayed in Figs. 6d and 6e, but ice virga in weak MPL signals is omitted because of possible relative large error in estimated extinction coefficients. The IWC image shows strong temporal variations and cellular structures. High IWC values generally correspond to relatively small D_{ge}, which suggests the strong variation in ice virga number concentration. Further understanding of this variation in number concentration is important to comprehend better the generation of ice particles in the water-dominated source cloud layer.

The retrieved LWP and r_{eff} for the supercooled water cloud component are presented in Figs. 8a and 8b. The r_{eff} ranges from 4 to 7.5 μm as LWP changes from 2
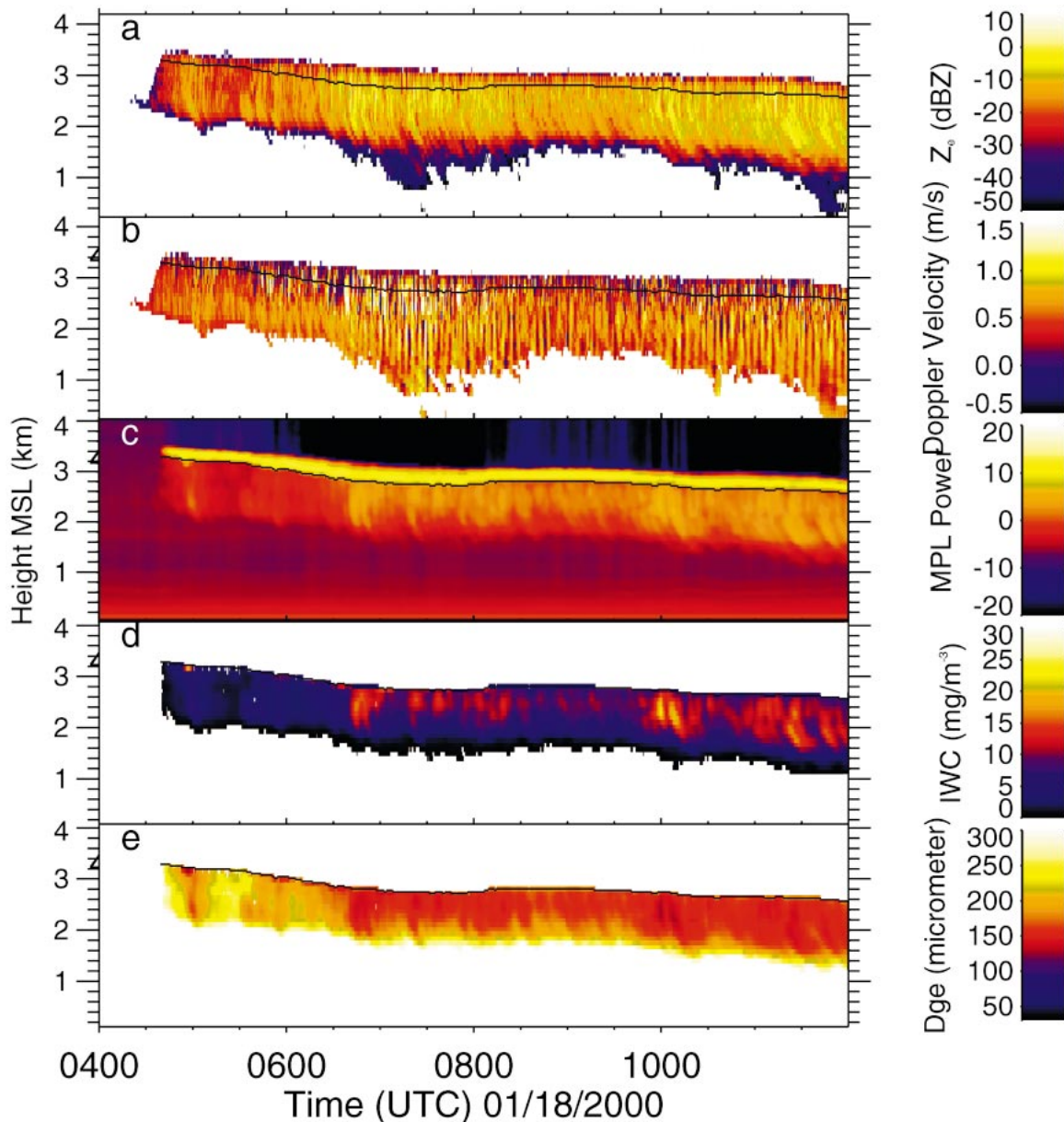
FIG. 6. Display of (a) Z_e, (b) mean Doppler velocity, and (c) MPL return power, and the (d) retrieved IWC and (e) D_{ge} of ice virga between 0400 and 1200 UTC 18 Jan 2000 at the NSA CART site. Note the black lines in (a), (b), and (c), which represent the supercooled water–dominated cloud base determined from MPL measurements.

to 12 g m^{-2}. For comparison, LWP values retrieved from the MWR measurements are shown in Fig. 8a as the dashed line, and it suggests a clear-sky bias as large as 10 g m^{-2} at 0430 UTC when no clouds are present. This bias is comparable to the maximum value of retrieved LWP. It is also clear that the pattern of LWP variations is different between them, indicating large uncertainties for the low LWP values in MWR retrievals. An inhomogeneous nature of the precipitating altocumulus is revealed by the variations of LWP and r_{eff}, as well as by the ice virga properties. For adiabatic water clouds, LWP is proportional to the square of the cloud-

layer thickness. The variations in LWP are consistent with the change of water cloud thickness indicated by the strong MPL returns.

As mentioned in section 3, τ can be estimated from lidar measurements and from retrieved LWP and r_{eff} data. A comparison of the results of the two methods (Fig. 8c) can be used to validate the retrieved LWP and r_{eff}. The agreement is good except for two strongly attenuating periods from 0630 to 0800 and from 1020 to 1150 UTC, which are clearly identified in the MPL power display in Fig. 6c (note lower background above dense layer). The optical depth of the ice virga is given
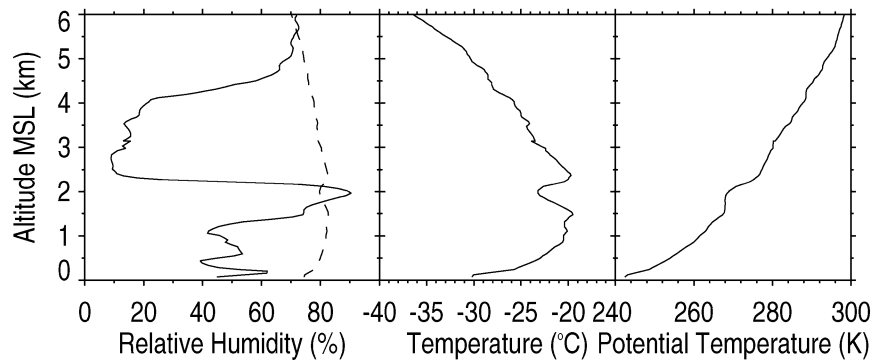
FIG. 7. Relative humidity with respect to water, temperature, and potential temperature profiles from a radiosonde at 1831 UTC 18 Jan 2000, where the dashed line is ice saturation relative humidity.
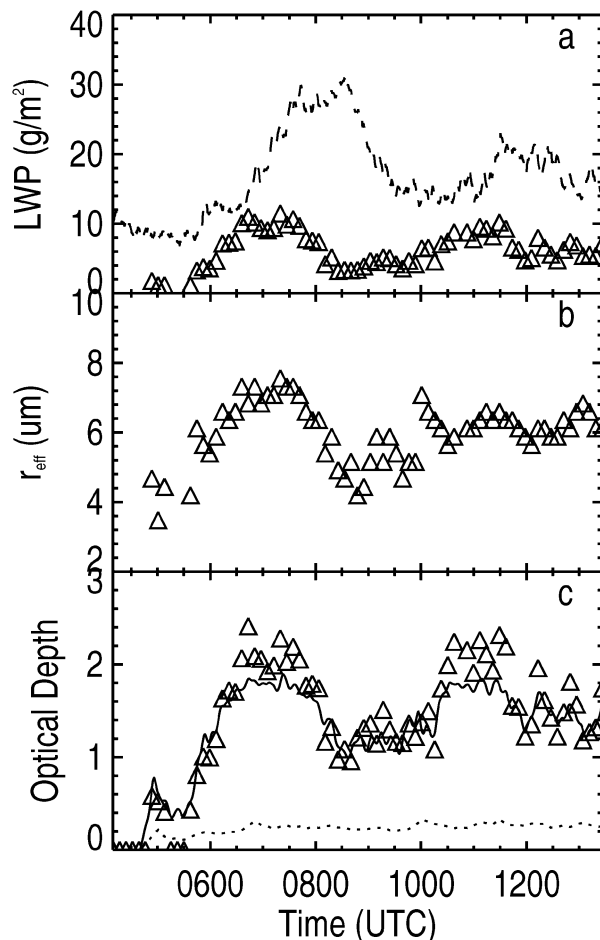
by the dashed line. Though it is only about one-tenth of the water-layer optical depth, its contribution to the downwelling IR radiance is important for the retrieval of the water-dominated source cloud properties.

b. 26 November 1996 at the SGP CART site

The second case is from 26 November 1996 at the SGP CART site, and Fig. 9 shows the evolution of the cloud with lidar scattering ratio (LSR; defined as the ratio of total backscattering coefficient to Rayleigh backscattering coefficient) and linear depolarization ratio (LDR; defined as the ratio of the measured perpendicular to parallel backscatter intensities, with respect to the transmitter polarization axis) measured by the Raman lidar and Z_e from MMCR. In the LSR display, the geometrically thin layer with LSR > 5 (white) indicates the supercooled water layer, which corresponds to a region with low LDR and small Z_e because of the relatively small size of the water droplets. The precipitating ice virga is associated with large Z_e, relatively high LDR, and small LSR.

Relative humidity, temperature, and potential temperature profiles from a CART radiosonde at 2028 UTC are presented in Fig. 10. A constant potential temperature region below 6 km suggests that the supercooled water layer is located at the top of a moist stable layer with a temperature of approximately −24°C. A 3°C temperature inversion at cloud top prohibits the further vertical development of clouds under a weak updraft situation. The ice-saturated relative humidity (dashed line) indicates that there is an ice-saturated region for the further growth of ice crystals as they are precipitating from the supercooled water–dominated source cloud.

Given in Fig. 11 are the retrieved LWP and r_{eff} for the supercooled water–dominated source cloud, which indicate r_{eff} of approximately 6 μm and LWP below 15 g m^{-2}. A comparison of LWP from the MWR measurements (dashed line in Fig. 11a) suggests a negative clear-sky bias of the MWR retrieval. Again, this comparison indicates that MWR measurements for low LWP

FIG. 8. The retrieved (a) LWP and (b) r_{eff} for the supercooled water clouds on 18 Jan 2000 at the NSA CART site. In (a), LWP estimated from MWR is given as a dashed line. (c) The comparison of visible optical depths for water-dominated cloud layer derived from MPL (solid line) and from LWP and r_{eff} (triangle symbols); the optical depth of ice virga is shown as a dashed line.
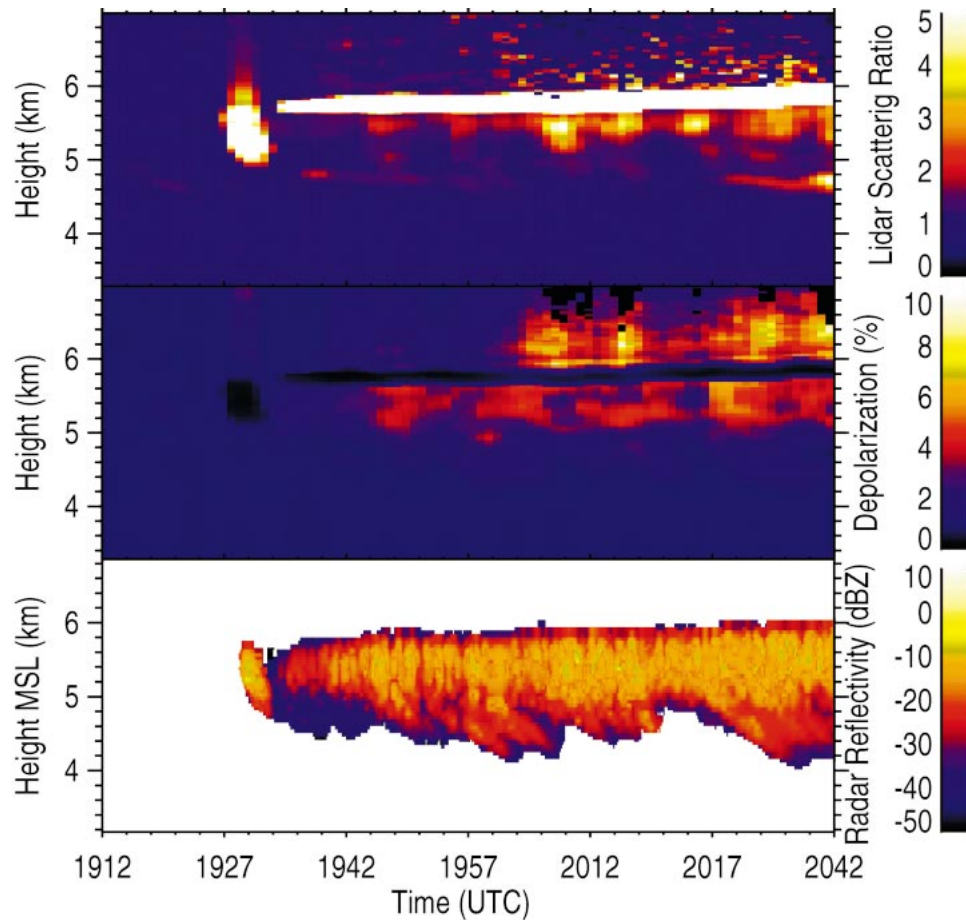
FIG. 9. The evolution of the clouds measured by MMCR and Raman lidar on 26 Nov 1996 at the SGP CART site: (top) lidar-scattering ratio, (middle) linear depolarization ratio, and (bottom) Z_e.

values are not reliable, and the retrieval from the AERI or other IR radiometer provides a good alternative for low LWP measurements.

The comparison between optical depths derived from the Raman lidar and the LWP and r_{eff} method is given in Fig. 11c. The τ estimated from both agree reasonably well. The differences may be partly due to the spatial separation (~100 m) and different fields of view be-

tween the Raman lidar and the AERI with regard to the inhomogeneity of the altocumulus clouds, but the small (negative) bias of the Raman data may have been caused by the effects of photon multiple-scattering activity. The optical depth of ice virga (dashed line) in this case is smaller than that of the first case. To understand the possible differences in mixed-phase cloud between different climate regions and clouds variability, we obvi-
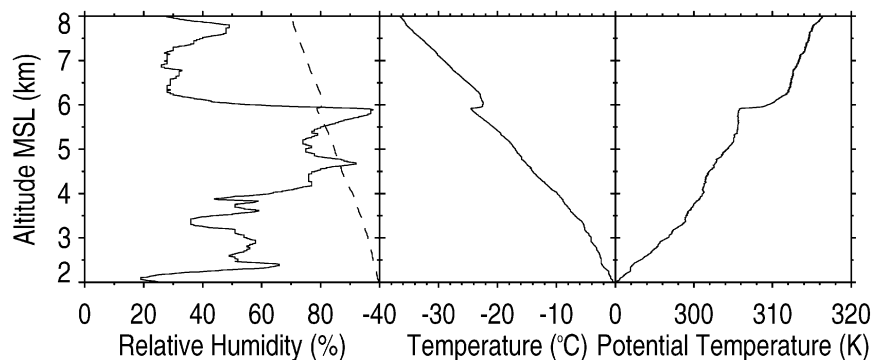

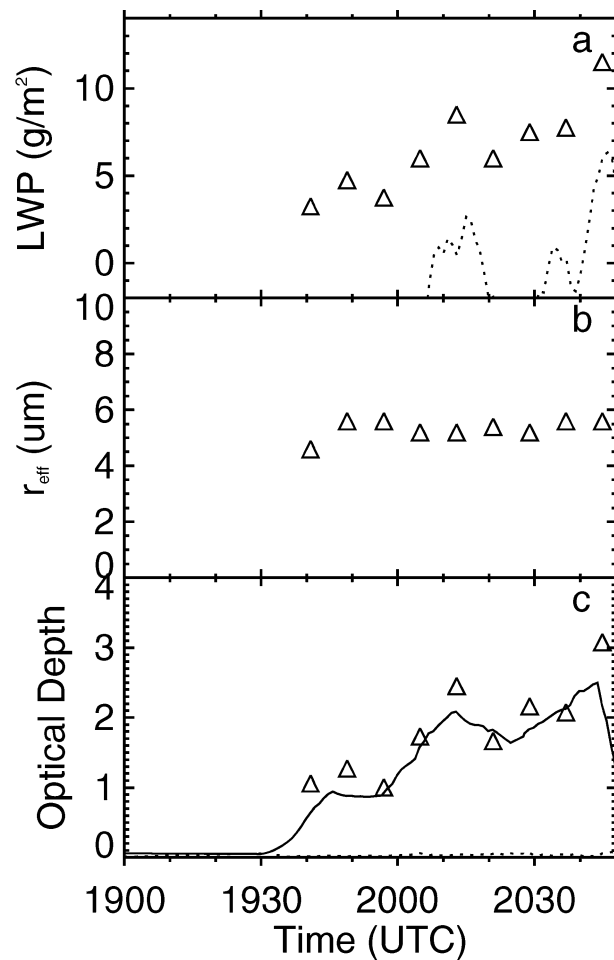FIG. 10. Same as Fig. 7, but at 2028 UTC 26 Nov 1996.

FIG. 11. Retrieved (a) LWP and (b) r_{eff} for supercooled water–dominated source cloud layer on 26 Nov 1996. In (a), LWP estimated from MWR is given as a dashed line. (c) The comparison of visible optical depths for the water-dominated cloud layer derived from Raman lidar (solid line) and from LWP and r_{eff} (triangle symbols); the optical depth of ice virga is shown as a dashed line.

ously have to study many more cases, including their large-scale and mesoscale environments.

Examples of measured Z_e and backscattering coefficient, and retrieved IWC and D_{ge} profiles are given in Fig. 12. A characteristically sharp increase in backscattering occurs when the laser pulse enters the dense water cloud above the ice virga (see the model results in Sassen et al. 1992). When compared with cirrus clouds at similar temperatures, the IWC in the ice virga is lower and D_{ge} is larger (Wang and Sassen 2002b), indicating a low concentration of ice particles in the virga. Combining the water vapor measurements from the Raman lidar and the Doppler velocity from MMCR, we may be able to study the fallout of ice from the water-dominated source cloud, the growth or sublimation of ice crystals below, and the maintenance of supercooled water clouds to understand better the mixed-

phase cloud processes. We will pursue these topics in future research.

5. Summary and conclusions

A combined active and passive remote sensing approach is presented for the study of supercooled liquid altocumulus cloud with ice virga. This cloud is a simple type of mixed-phase cloud in which the supercooled water–dominated source cloud is confined to the cloud top, with a deep ice-particle virga layer below. This common type of midlevel mixed-phase cloud is easily identified by combining lidar and cloud radar measurements because significant differences in the lidar and radar signals because of the substantial differences between water and ice cloud microphysical properties exist. Although the LWP in altocumulus is often too small for the MWR to detect, the variation of water imaginary index within the IR window region provides us with the capability to retrieve LWP from combined measurements of lidar, radar, and AERI.

First, we treat the virga as a cirruslike ice cloud and apply an existing lidar–radar algorithm to retrieve IWC and D_{ge} profiles. Then, an iterative approach is developed to retrieve supercooled water cloud properties by minimizing differences between observed IR radiances and the DISORT-calculated radiances at 12 selected wavelengths. The inputs for the DISORT calculations include cloud temperature determined from radiosonde temperature profile and lidar–radar-identified cloud height, a molecular absorption profile, and retrieved ice virga properties. A sound theoretical base and error analyses based on simulations indicate that this iterative approach provides reliable retrieval of LWP and layer-mean r_{eff} for supercooled water clouds with ice virga. One limitation of this approach is that it is only applicable to clouds with absorption optical depth of less than approximately 3 at the strongly absorbing IR wavelengths.

This multiple remote sensor approach is applied to two mixed-phase cloud case studies observed at the NSA and SGP CART sites. The results illustrate the capabilities of this approach to retrieve important microphysical properties needed to characterize this type of mixed-phase cloud radiatively. The good agreement between visible optical depths derived from lidar measurements and that estimated from retrieved LWP and r_{eff} provides a closure test for the accuracy of the mainly AERI-based supercooled water cloud retrieval. Combining these retrieved results with other measurements, such as a water vapor profile from Raman lidar and particle Doppler velocity from MMCR, we may study additional cloud microphysical processes. Applying this analysis approach to larger CART datasets to understand mixed-phase clouds and their possible differences in diverse climate regimes better is an ongoing goal to improve cloud parameterization in GCMs.
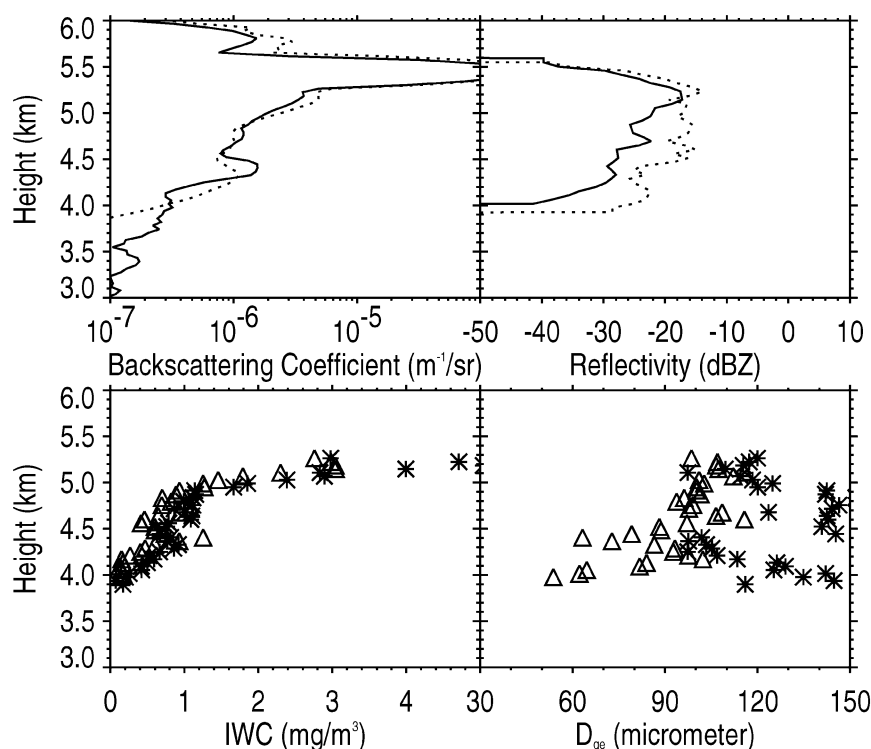
FIG. 12. Measured Z_e and lidar backscattering coefficient and retrieved IWC and D_{ge} profiles for ice virga at 1851 (solid line and triangle symbols) and 2000 UTC (dashed line and asterisk symbols) 26 Nov 1996.

REFERENCES

Ackerman, S. A., W. L. Smith, A. D. Collard, X. L. Ma, H. E. Revercomb, and R. O. Knuteson, 1995: Cirrus cloud properties derived from high spectral resolution infrared spectrometry during FIRE II. Part II: Aircraft HIS results. *J. Atmos. Sci.,* **52,** 4246–4263.

Baker, M. B., 1997: Cloud microphysics and climate. *Science,* **276,** 1072–1078.

Berk, A., L. S. Bernstein, G. P. Anderson, P. K. Acharya, D. C. Robertson, J. H. Chetwynd, and S. M. Adler-Golden, 1998: MODTRAN cloud and multiple scattering upgrades with application to AVIRIS. *Remote Sens. Environ.,* **65,** 367–375.

Cober, S. G., G. A. Isaac, A. V. Korolev, and J. W. Strapp, 2001: Assessing cloud-phase conditions. *J. Appl. Meteor.,* **40,** 1967–1983.

Comstock, J. M., and K. Sassen, 2001: Retrieval of cirrus cloud radiative and backscattering properties using combined lidar and infrared radiometer (LIRAD) measurements. *J. Atmos. Oceanic Technol.,* **18,** 1658–1673.

DeSlover, H. D., W. L. Smith, P. K. Piirone, and E. W. Eloranta, 1999: A methodology for measuring cirrus cloud visible-to-infrared spectral optical depth ratios. *J. Atmos. Oceanic Technol.,* **16,** 251–262.

Field, P. R., 1999: Aircraft observations of ice crystal evolution in altostratus cloud. *J. Atmos. Sci.,* **56,** 1925–1941.

Fleishauer, R. P., V. E. Larson, and T. H. Vonder Haar, 2002: Observed microphysical structure of midlevel, mixed-phase clouds. *J. Atmos. Sci.,* **59,** 1779–1804.

Fowler, L. D., D. A. Randall, and S. A. Rutledge, 1996: Liquid and ice cloud microphysics in the CSU general circulation model. Part I: Model description and simulated microphysical processes. *J. Climate,* **9,** 489–529.

Fu, Q., P. Yang, and W. B. Sun, 1998: An accurate parameterization of the infrared radiative properties of cirrus clouds for climate models. *J. Climate,* **11,** 2223–2237.

Gedzelman, S. D., 1988: In praise of altocumulus. *Weatherwise,* **41,** 143–149.

Goldsmith, J., B. Forest, S. Bisson, and D. Turner, 1998: Turn-key Raman lidar for profiling atmospheric water vapor, clouds, and aerosols. *Appl. Opt.,* **37,** 4979–4990.

Gregory, D., and D. Morris, 1996: The sensitivity of climate simulation to the specification of mixed phase clouds. *Climate Dyn.,* **12,** 641–651.

Heymsfield, A. J., L. M. Milosevich, A. Slingo, K. Sassen, and D. O'C. Starr, 1991: An observational and theoretical study of highly supercooled altocumulus. *J. Atmos. Sci.,* **48,** 923–945.

Hobbs, P. V., and A. L. Rangno, 1985: Ice particle concentrations in clouds. *J. Atmos. Sci.,* **42,** 2523–2549.

Hogg, D. C., and Coauthors, 1983: A steerable dual-channel microwave radiometer for measurement of water and liquid in the troposphere. *J. Climate Appl. Meteor.,* **22,** 789–806.

Lawson, R. P., B. A. Baker, C. G. Schmitt, and T. L. Jensen, 2001: An overview of microphysical properties of arctic clouds observed in May and July during FIRE ACE. *J. Geophys. Res.,* **106,** 14 989–15 014.

Li, Z.-X., and H. Le Treut, 1992: Cloud-radiation feedbacks in a

general circulation model and their dependence on cloud modeling assumptions. *Climate Dyn.,* **7,** 133–139.

Mace, G. G., T. A. Ackerman, P. Minnis, and D. F. Young, 1998: Cirrus layer microphysical properties derived from surface-based millimeter radar and infrared interferometer data. *J. Geophys. Res.,* **103,** 23 027–23 216.

Moran, K. P., B. E. Martner, M. J. Post, R. A. Kropfli, D. C. Welsh, and K. B. Widener, 1998: An unattended cloud-profiling radar for use in climate research. *Bull. Amer. Meteor. Soc.,* **79,** 443–455.

Pinto, J. O., 1998: Autumnal mixed-phase cloudy boundary layers in the Arctic. *J. Atmos. Sci.,* **55,** 2016–2037.

Rauber, R. M., and A. Tokay, 1991: An explanation for the existence of supercooled water at the tops of cold clouds. *J. Atmos. Sci.,* **48,** 1005–1023.

Sassen, K., 1991: Aircraft produced ice particles in a highly supercooled altocumulus cloud. *J. Appl. Meteor.,* **30,** 765–775.

——, and J. M. Comstock, 2001: A midlatitude cirrus cloud climatology from the Facility for Atmospheric Remote Sensing. Part III: Radiative properties. *J. Atmos. Sci.,* **58,** 2113–2127.

——, H. Zhao, and G. C. Dodd, 1992: Simulated polarization diversity lidar returns from water and precipitating mixed phase clouds. *Appl. Opt.,* **31,** 2914–2923.

——, J. M. Comstock, Z. Wang, and G. G. Mace, 2001: Cloud and aerosol research capabilities at FARS: The Facility for Atmospheric Remote Sensing. *Bull. Amer. Meteor. Soc.,* **82,** 1119–1138.

Sauvageot, H., 1996: Retrieval of vertical profiles of liquid water and ice content in mixed clouds from Doppler radar and microwave radiometer measurements. *J. Appl. Meteor.,* **35,** 14–23.

Smith, W. L., X. L. Ma, S. A. Ackerman, H. E. Revercomb, and R. O. Knuteson, 1993: Remote sensing cloud properties from high spectral resolution infrared observations. *J. Atmos. Sci.,* **50,** 1708–1720.

Spinhirne, J. D., 1993: Micro-pulse lidar. *IEEE Trans. Geosci. Remote Sens.,* **31,** 48–55.

Stamnes, K., S.-C. Tasy, W. Wiscombe, and K. Jayaweera, 1988: A numerically stable algorithm for discrete-ordinate-method ra-

diative transfer in multiple scattering and emitting layered media. *Appl. Opt.,* **27,** 2502–2509.

Stephens, G. L., S. Tsay, P. W. Stackhouse, and P. J. Flatau, 1990: The relevance of the microphysical and radiative properties of cirrus clouds to climate and climatic feedback. *J. Atmos. Sci.,* **47,** 1742–1753.

Stokes, G. M., and S. E. Schwartz, 1994: The Atmospheric Radiation Measurement (ARM) Program: Programmatic background and design of the Cloud and Radiation Test Bed. *Bull. Amer. Meteor. Soc.,* **75,** 1201–1221.

Strabala, K. I., S. A. Ackerman, and W. P. Menzel, 1994: Cloud properties inferred from 8–12-μm data. *J. Appl. Meteor.,* **33,** 212–229.

Sun, Z., and K. P. Shine, 1994: Studies of the radiative properties of ice and mixed-phase clouds. *Quart. J. Roy. Meteor. Soc.,* **120,** 111–137.

Turner, D. D., S. A. Ackerman, B. A. Baum, and P. Yang, 2003: Cloud phase determination using ground-based AERI observations at SHEBA. *J. Appl. Meteor.,* **42,** 701–715.

Vivekanandan, J., B. E. Martner, M. K. Politovich, and G. Zhang, 1999: Retrieval of atmospheric liquid and ice characteristics using dual-wavelength radar observations. *IEEE Trans. Geosci. Remote Sens.,* **37,** 2325–2334.

Wang, Z., and K. Sassen, 2001: Cloud type and macrophysical property retrieval using multiple remote sensors. *J. Appl. Meteor.,* **40,** 1665–1682.

——, and ——, 2002a: Cirrus cloud microphysical property retrieval using lidar and radar measurements. Part I: Algorithm description and comparison with in situ data. *J. Appl. Meteor.,* **41,** 218–229.

——, and ——, 2002b: Cirrus cloud microphysical property retrieval using lidar and radar measurements. Part II: Midlatitude cirrus microphysical and radiative properties. *J. Atmos. Sci.,* **59,** 2291–2302.

Whiteman, D. N., S. H. Melfi, and R. A. Ferrare, 1992: Raman lidar system for the measurement of water vapor and aerosols in the earth's atmosphere. *Appl. Opt.,* **31,** 3068–3082.

Young, S. A., C. M. R. Platt, R. T. Austin, and G. R. Patterson, 2000: Optical properties and phase of some midlatitude, midlevel clouds in ECLIPS. *J. Appl. Meteor.,* **39,** 135–153.